COMMUNICATIONS IN NUMERICAL METHODS IN ENGINEERING
*Commun. Numer. Meth. Engng* (in press)
Published online in Wiley InterScience (www.interscience.wiley.com). DOI: 10.1002/cnm.1021

# Charge distribution on narrow MEMS beams of nearly square cross-section

Hui Chen and Subrata Mukherjee*, †

*Department of Theoretical and Applied Mechanics, Kimball Hall, Cornell University, Ithaca, NY 14853, U.S.A.*

SUMMARY

The subject of this paper is the calculation of charge distribution on the surfaces of thin conducting microelectromechanical systems beams, of nearly square cross-section, in electrostatic problems, by the boundary element method (BEM). A line model of a beam is proposed here. This model overcomes the problem of dealing with nearly singular matrices that occur when the standard BEM is applied to very thin features (objects or gaps). This new approach is also very efficient. Numerical results are presented for selected examples. Copyright © 2007 John Wiley & Sons, Ltd.

Received 24 March 2006; Revised 17 April 2007; Accepted 18 May 2007

KEY WORDS: charge distribution; microelectromechanical systems; narrow beams; boundary element method

## 1. INTRODUCTION

Microelectromechanical systems (MEMS) have demonstrated important applications in a wide variety of industries including mechanical and aerospace, medicine, communications, information technology, etc.

Numerical simulation of electrically actuated MEMS devices has been carried out for nearly 15 years by using the boundary element method (BEM—see e.g. [1–5]) to model the exterior electric field and the finite element method (FEM—see e.g. [6–8]) to model the deformation of the structure. The commercial software package MEMCAD [9], for example, uses the commercial FEM software package ABAQUS for mechanical analysis, together with a BEM code FastCap [10] for the electric field analysis. Other examples of such work are [11–14], as well as [9, 15, 16] for dynamic analysis of MEMS.

*Correspondence to: Subrata Mukherjee, Department of Theoretical and Applied Mechanics, Kimball Hall, Cornell University, Ithaca, NY 14853, U.S.A.
†E-mail: sm85@cornell.edu

Contract/grant sponsor: National Science Foundation; contract/grant number: CMS-0508466

Copyright © 2007 John Wiley & Sons, Ltd.

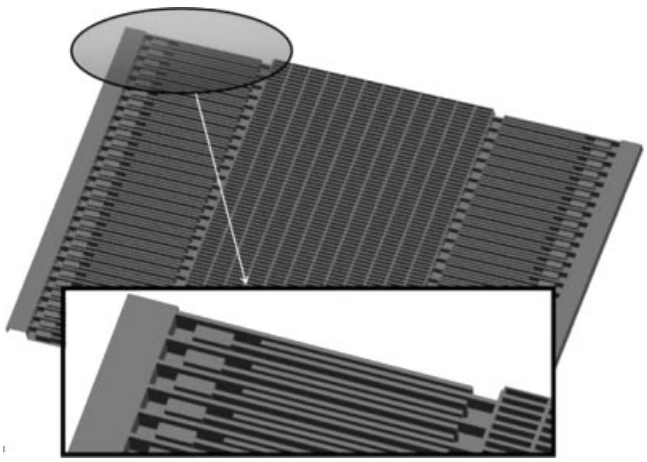

Figure 1. Parallel plate resonator: geometry and detail of the parallel plate fingers (from [17]).

Many applications in MEMS require BEM analysis of the electric field exterior to thin conducting objects. In the context of MEMS with very thin beams or plates (see Figure 1), a convenient way to model such a problem is to assume plates with vanishing thickness and solve for the sum of the charges on the upper and lower surfaces of each plate [18]. The standard boundary integral equation (BIE) with a weak singular kernel is used in [18] and this approach works well for determining, for example, the capacitance of a parallel plate capacitor. For MEMS calculations, however, one must obtain the charge densities separately on the upper and lower surfaces of a plate since the traction at a surface point on a plate depends on the square of the charge density at that point. The gradient BIE is employed in [19] to obtain these charge densities separately. The formulation given in [19] is a BEM scheme that is particularly well suited for MEMS analysis of very thin plates—for $h/L \leqslant 0.001$—in terms of the length $L$ (of a side of a square plate) and its thickness $h$. A similar approach has also been developed for MEMS with very thin beams (2-D problems) [20]. Similar work has also been reported recently by Chuyan *et al*. [21] in the context of determining fringing fields and levitating forces for 2-D beam-shaped conductors in MEMS combdrives. A fully coupled BEM/FEM MEMS calculation with very thin plates has been completed recently [22]. See also [23] for an application of the thin plate idea for modelling damping forces on MEMS with thin plates.

Turning now to nanoelectromechanical systems (NEMS), two recent studies [24, 25] have considered the 3-D problem of charge distribution on conducting carbon nanotubes (CNTs). Both the studies have employed the BEM. The former applies the full 3-D BEM, while the latter takes advantage of the long thin geometry of a nanotube and proposes a reduced 3-D or line model for a CNT. This approach effectively produces a 1-D rather than a 3-D model for a CNT. Numerical results presented in [25] are most encouraging.

Many MEMS applications involve narrow beams of length around hundreds of μm, and with cross-sections that are square (or nearly so) with side around 1 μm. Batra *et al.* [26], for example, consider pull-in of such micro-beams. In this paper, they model the external electric field with the standard BEM (called the method of moments in [18]), with a 2-D model of a beam cross-section. In contrast, a line model of a 3-D narrow beam is developed in the present work, in a manner

Copyright © 2007 John Wiley & Sons, Ltd.

DOI: 10.1002/cnm

analogous to the line model for a CNT in [25]. The primary contribution of the present work, therefore, is the development of a line model of a narrow beam, of nearly square cross-section, in a 3-D region (called a reduced 3-D model). As before [19, 20, 25], this model overcomes the problem of dealing with nearly singular matrices that occur when the standard BEM is applied to very thin gaps. It also greatly simplifies the BEM calculations and is computationally very efficient. Finally, the actual charge distribution on the entire surface of a narrow beam can be recovered *at a post-processing step*!

The present paper is organized as follows. The notion of an 'equivalent' circular cross-section to replace a rectangular cross-section of a narrow beam is presented first. A BIE is presented next for an infinite region containing one thin beam of circular cross-section and the (infinite) ground plane. (This BIE is the same as the one for CNTs presented before in [25].) The ground is modelled indirectly by adding a suitable image beam in the computational domain. This approach of modelling the ground plane is quite standard (see e.g. [19, 20, 24]). An alternate ground model is available in [27].

The gradient BIE is presented next. This equation is useful for determining the charge distribution around a beam cross-section as a post-processing step. This section is followed by numerical results for the charge density, per unit length on a narrow beam, from this reduced 3-D model. These numerical results are compared with the analytical solution for charge distribution along a thin tube (of circular cross-section) of infinite length [28, p. 159], and also with numerical results for a 2-D cross-section BEM model. Numerical results for the charge distribution, per unit area on a beam surface, obtained from the gradient BIE, follow. A Concluding Remarks section completes the paper.

## 2. BIEs IN SEMI-INFINITE 3-D REGION CONTAINING A NARROW CONDUCTING BEAM AND THE GROUND

### *2.1. The problem*

Consider the situation shown in Figure 2 with two parallel narrow beams (the physical beam and a parallel image beam). Of interest is the solution of the following Dirichlet problem for Laplace's equation:

$$\nabla^2\phi(\mathbf{x}) = 0, \quad \mathbf{x} \in B, \quad \phi(\mathbf{x}) \text{ prescribed for } \mathbf{x} \in \partial B \tag{1}$$

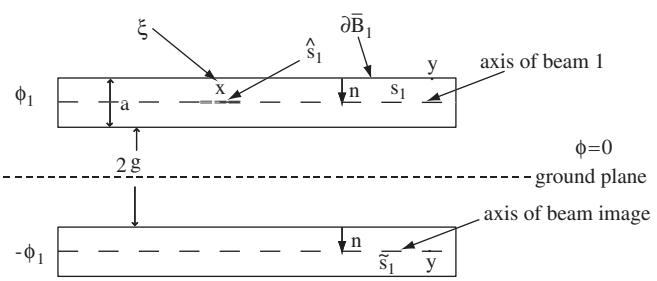


Figure 2. Narrow beam with image.

Copyright © 2007 John Wiley & Sons, Ltd.

DOI: 10.1002/cnm

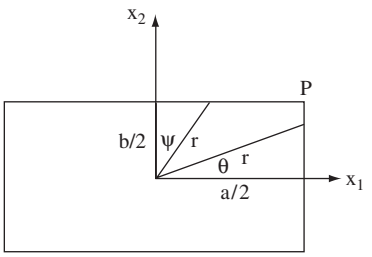


Figure 3. Calculation of radius of equivalent circular cross-section beam.

where $\phi$ is the potential and $B$ is the region *exterior* to the two beams, each of length $L$ and nearly square cross-section $a \times b$. The total surface of the two beams is $\partial B$ and the unit normal $\mathbf{n}$ to $\partial B$ is defined to point away from $B$ (i.e. into a beam).

### 2.2. *Equivalent circular cross-section*

An equivalent circular cross-section replacement beam is necessary in order to apply the simplified methods presented in [25]. The distance between the centre of a beam and the ground is kept the same when the actual beam cross-section is replaced by a circular one.

There are, of course, many ways to choose the radius $\rho$ of this replacement circular cross-section. Examples are equal cross-section area, equal cross-section perimeter, etc. In view of the $1/r$ behaviour of the 3-D Laplace equation kernel, the following choice has been made:

$$1/\rho = E(1/r) \tag{2}$$

where $E$ denotes the expected (average) value of the Euclidean distance between the centre and a point on the boundary of the rectangular cross-section of a beam. This choice is made because it is elegant and is justified *a posteriori*.

Referring to Figure 3, with $r(\theta) = a/(2\cos(\theta))$, $r(\psi) = b/(2\cos(\psi))$ one gets:

$$\frac{1}{\rho} = \frac{2}{\pi}\int_0^{\theta_P} \frac{2\cos(\theta)}{a}\,\mathrm{d}\theta + \frac{2}{\pi}\int_0^{\psi_P} \frac{2\cos(\psi)}{b}\,\mathrm{d}\psi \tag{3}$$

With $\tan(\theta_P) = b/a$, $\tan(\psi_P) = a/b$, one gets:

$$\rho = \frac{\pi ab}{4\sqrt{a^2+b^2}} \tag{4}$$

For a square cross-section with side $a$, $\rho = 0.555a$. Square cross-sections are depicted in Figure 4, but nearly square rectangular cross-sections can also be handled by the methods proposed in this paper. Please note that $g_c + \rho = g + a/2$ in Figure 4. Here, $2g$ is the physical gap between the square cross-sections of the real beams and $2g_c$ is the gap between the replacement circles.

Copyright © 2007 John Wiley & Sons, Ltd.

DOI: 10.1002/cnm

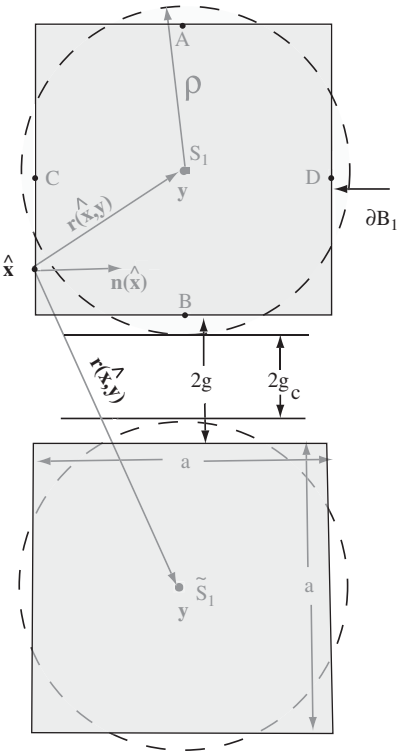


Figure 4. Beam cross-section with image. A dotted circle of radius $\rho$ represents the replacement of a square by a circle for the calculation of the charge density per unit length, $q$, along a beam. Note that $g_c + \rho = g + a/2$.

### *2.3. Regular BIE—source point approaching the beam axis $s_1$*

Narrow beams with equivalent circular cross-sections are considered in this section.

For a source point $\boldsymbol{\xi} \in B \to \mathbf{x} \in \hat{s}_1 \subset s_1$ (see Figures 2 and 4), one has

$$\phi(\mathbf{x}) = \int_{\partial \tilde{B}_1} \frac{q(\mathbf{y})}{4\pi\varepsilon r(\mathbf{x}, \mathbf{y})}\, \mathrm{d}\ell(\mathbf{y}) + \int_{\tilde{s}_1} \frac{q(\mathbf{y})}{4\pi\varepsilon r(\mathbf{x}, \mathbf{y})}\, \mathrm{d}\ell(\mathbf{y}), \quad \mathbf{x} \in \hat{s}_1 \subset s_1 \tag{5}$$

with

$$q(\mathbf{y}) = \int_0^{2\pi} \sigma(y_3, \rho, \theta)\rho\, \mathrm{d}\theta, \quad y_3 \in s_1 \text{ or } \tilde{s}_1 \tag{6}$$

Here, $\sigma$ is the charge density, per unit surface area, on the beam surface and $q$ is the charge density, per unit length, on the beam axis $s_1$. The axial coordinate for a straight beam is $y_3$. For a bent beam, $y_3$ must be replaced by the arc length coordinate $\ell$ along the (bent) axis of the tube and the integration in (6) must be carried out on a planar cross-section of the tube that is normal to the local arc length direction.

It is first noted that the source point $\mathbf{x}$ in (5) lies inside rather than on the surface of a beam. The potential at any such point $\mathbf{x}$, however, is known (it is the same as on the beam surface) and

Copyright © 2007 John Wiley & Sons, Ltd.

DOI: 10.1002/cnm

can be used as a 'boundary' condition. Also, both beams are assumed to be very thin and a line model is used for each of them.

The starting point for the first integral on the right-hand side of (5) is the double integral

$$\int_{\partial \bar{B}_1} \mathrm{d}\ell(\mathbf{y}) \int_0^{2\pi} \frac{\sigma(\mathbf{y})\rho \, \mathrm{d}\theta}{4\pi\varepsilon r(\mathbf{x}, \mathbf{y})} \tag{7}$$

where $\partial \bar{B}_1$ is a line on the beam surface $\partial B_1$ which is parallel to the beam axis $s_1$. In view of (7), and the fact that $r(\mathbf{x}, \mathbf{y})$ in this case is, in fact, independent of $\mathbf{y}$ (and therefore of $\theta$), the first term on the right-hand side of (5) is exact. The second integral on the right-hand side of (5) follows from the assumption that $g \gg \rho$ (where $g$ is the gap between the nanotube and the ground and $\rho$ in the radius of an equivalent beam of circular cross-section (see Figures 2 and 4). Therefore, one has $r(\mathbf{x}, \mathbf{y}) \gg \rho$ and it is assumed that $r$ is independent of $\theta$ with the field point $\mathbf{y}$ moving on the boundary of a cross-section of the image beam. Next, $r(\mathbf{x}, \mathbf{y})$ is approximated to be the distance from $\mathbf{x} \in s_1$ and $\mathbf{y} \in \tilde{s}_1$. Exactly how large $g$ has to be compared to $\rho$ is discussed in [25].

The first integral in (5) is nearly strongly singular and the second is regular. An evaluation procedure for the first integral is discussed in [25].

Given $\phi$, Equation (5) can be solved for $q(\mathbf{y})$ on $s_1$.

### *2.4. Gradient BIE—source point approaching the surface $\partial B_1$ of a beam of square cross-section*

Let $\boldsymbol{\xi} \to \hat{\mathbf{x}} \in \partial B_1$ (see Figure 4). Now, one uses (5) and (8) for the charge density on a beam surface:

$$\sigma(\mathbf{x}) = \varepsilon \frac{\partial \phi}{\partial n}(\mathbf{x}) = \varepsilon \mathbf{n}(\mathbf{x}) \cdot [\nabla_{\boldsymbol{\xi}} \phi(\boldsymbol{\xi})]_{\boldsymbol{\xi}=\mathbf{x}} \tag{8}$$

The resulting gradient BIE (see Figure 4) is

$$\sigma(\hat{\mathbf{x}}) = \int_{s_1 \cup \tilde{s}_1} \frac{\mathbf{r}(\hat{\mathbf{x}}, \mathbf{y}) \cdot \mathbf{n}(\hat{\mathbf{x}}) q(\mathbf{y})}{4\pi r^3(\hat{\mathbf{x}}, \mathbf{y})} \, \mathrm{d}\ell(\mathbf{y}), \quad \hat{\mathbf{x}} \in \partial B_{N_1} \tag{9}$$

Please note that the one now reverts back to the actual square cross-section narrow beams. Square cross-section beams are considered in this section for illustrating the present approach. Rectangular cross-section beams can also be included by a simple extension of the present idea.

With $q(\mathbf{y})$ known, (9) can be used, *as a post-processing step*, to find the charge density distribution $\sigma(\mathbf{x})$ on the outer surface of the beam with axis $s_1$.

Again, a line model is assumed for each of the beams, i.e. the integrals on their surfaces are replaced by those on their axes.

The integral on $s_1$ in (9) is nearly hypersingular. Its evaluation is discussed in Section 2.4.1. The integral on $\tilde{s}_1$ is regular.

*2.4.1. Evaluation of integral on $s_1$ in (9).* This procedure, for the square cross-sections shown in Figure 4, closely follows the derivation for circular cross-sections in [25].

Copyright © 2007 John Wiley & Sons, Ltd.

DOI: 10.1002/cnm

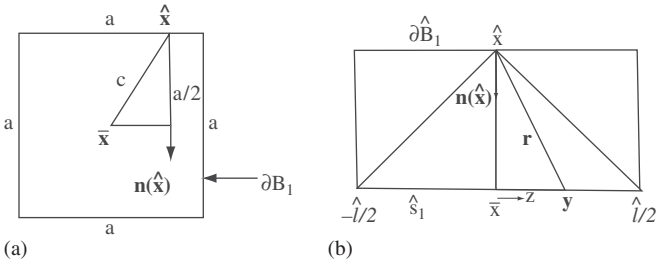


Figure 5. Evaluation of the third integral in (10).

This nearly hypersingular integral is first written as

$$\begin{aligned}
&\int_{s_1} \frac{\mathbf{r}(\hat{\mathbf{x}},\mathbf{y})\cdot\mathbf{n}(\hat{\mathbf{x}})q(\mathbf{y})}{4\pi r^3(\hat{\mathbf{x}},\mathbf{y})}\,\mathrm{d}\ell(\mathbf{y})\\
&\quad=\int_{s_1-\hat{s}_1} \frac{\mathbf{r}(\hat{\mathbf{x}},\mathbf{y})\cdot\mathbf{n}(\hat{\mathbf{x}})q(\mathbf{y})}{4\pi r^3(\hat{\mathbf{x}},\mathbf{y})}\,\mathrm{d}\ell(\mathbf{y})\\
&\qquad+\int_{\hat{s}_1} \frac{\mathbf{r}(\hat{\mathbf{x}},\mathbf{y})\cdot\mathbf{n}(\hat{\mathbf{x}})[q(\mathbf{y})-q(\bar{\mathbf{x}})-q'(\bar{\mathbf{x}})(\mathbf{y}-\bar{\mathbf{x}})]}{4\pi r^3(\hat{\mathbf{x}},\mathbf{y})}\,\mathrm{d}\ell(\mathbf{y})+q(\bar{\mathbf{x}})\int_{\hat{s}_1} \frac{\mathbf{r}(\hat{\mathbf{x}},\mathbf{y})\cdot\mathbf{n}(\hat{\mathbf{x}})}{4\pi r^3(\hat{\mathbf{x}},\mathbf{y})}\,\mathrm{d}\ell(\mathbf{y})\\
&\qquad+q'(\bar{\mathbf{x}})\int_{\hat{s}_1} \frac{\mathbf{r}(\hat{\mathbf{x}},\mathbf{y})\cdot\mathbf{n}(\hat{\mathbf{x}})(\mathbf{y}-\bar{\mathbf{x}})}{4\pi r^3(\hat{\mathbf{x}},\mathbf{y})}\,\mathrm{d}\ell(\mathbf{y}),\quad \hat{\mathbf{x}}\in\partial\hat{B}_1\subset\partial B_1
\end{aligned}\tag{10}$$

where $\bar{\mathbf{x}}\in\hat{s}_1$ is closest to $\hat{\mathbf{x}}\in\partial B_1$ (see Figure 5). Also, $\hat{\mathbf{x}}$ is at the mid-point of the segment $\partial\hat{B}_1$ of $\partial B_1$. This is sufficient since (9) is a post-processing step.

Referring to Figure 5, for a piecewise quadratic approximation for $q(\mathbf{y})$, the second integral on the right-hand side of (10) (using the Taylor series for $q(\mathbf{y})$ about $\bar{\mathbf{x}}$) becomes:

$$\frac{q''(\bar{\mathbf{x}})}{16\pi}\int_{-\hat{\ell}/2}^{\hat{\ell}/2}\frac{az^2\,\mathrm{d}z}{(z^2+c^2)^{3/2}}\tag{11}$$

This integral can be evaluated analytically.

Again referring to Figure 5, the third integral on the right-hand side of (10) becomes:

$$q(\bar{\mathbf{x}})\int_{\hat{s}_1}\frac{\mathbf{r}(\hat{\mathbf{x}},\mathbf{y})\cdot\mathbf{n}(\hat{\mathbf{x}})}{4\pi r^3(\hat{\mathbf{x}},\mathbf{y})}\,\mathrm{d}\ell(\mathbf{y})=\frac{q(\bar{\mathbf{x}})}{8\pi}\int_{-\hat{\ell}/2}^{\hat{\ell}/2}\frac{a\,\mathrm{d}z}{(z^2+c^2)^{3/2}}\tag{12}$$

This integral can be evaluated analytically. The last integral on the right-hand side of (10) is:

$$q'(\bar{\mathbf{x}})\int_{\hat{s}_1}\frac{\mathbf{r}(\hat{\mathbf{x}},\mathbf{y})\cdot\mathbf{n}(\hat{\mathbf{x}})(\mathbf{y}-\bar{\mathbf{x}})}{4\pi r^3(\hat{\mathbf{x}},\mathbf{y})}\,\mathrm{d}\ell(\mathbf{y})=\frac{q'(\bar{\mathbf{x}})}{8\pi}\int_{-\hat{\ell}/2}^{\hat{\ell}/2}\frac{az\,\mathrm{d}z}{(z^2+c^2)^{3/2}}=0\tag{13}$$

Copyright © 2007 John Wiley & Sons, Ltd.

DOI: 10.1002/cnm

Finally, (10) has the simple form:

$$\int_{s_1} \frac{\mathbf{r}(\hat{\mathbf{x}}, \mathbf{y}) \cdot \mathbf{n}(\hat{\mathbf{x}}) q(\mathbf{y})}{4\pi r^3(\hat{\mathbf{x}}, \mathbf{y})} \, \mathrm{d}\ell(\mathbf{y}) = \int_{s_1 - \hat{s}_1} \frac{a q(\mathbf{y})}{8\pi r^3(\hat{\mathbf{x}}, \mathbf{y})} \, \mathrm{d}\ell(\mathbf{y}) + \frac{q''(\bar{\mathbf{x}})}{16\pi} \int_{-\hat{\ell}/2}^{\hat{\ell}/2} \frac{a z^2 \, \mathrm{d}z}{(z^2 + c^2)^{3/2}} + \frac{q(\bar{\mathbf{x}})}{8\pi} \int_{-\hat{\ell}/2}^{\hat{\ell}/2} \frac{a \, \mathrm{d}z}{(z^2 + c^2)^{3/2}}, \quad \hat{\mathbf{x}} \in \partial \hat{B}_1 \subset \partial B_1 \tag{14}$$

where $c = r(\hat{\mathbf{x}}, \bar{\mathbf{x}})$.

For the numerical calculations, $\hat{\ell}$ in Figure 5 is taken to be the length of a boundary element.

## 3. RESULTS

### *3.1. Analytical solutions for sample problems*

Analytical solutions for $q$ and $\sigma$, for two infinite conductive parallel (*cylindrical*) tubes with potentials $\phi$ and $-\phi$, are given first. (See Figures 6 and 2 that show two parallel finite narrow beams.)

For a *circular cross-section tube* of radius $\rho$, separated by gap $2g$, one has [24, 28] (see also Figure 10 in [25]):

$$q = \frac{2\pi\varepsilon\phi}{\cosh^{-1}(1 + g/\rho)} \tag{15}$$

The next problem concerns *charge densities around beams of square cross-section*.

Referring to Figures 7(a) and 6, analytical solutions can be obtained for the charge densities $\sigma(A)$, $\sigma(B)$ and $\sigma(C) = \sigma(D)$.

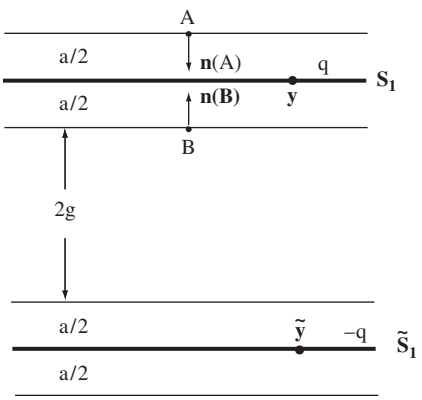


Figure 6. Two parallel narrow beams of infinite length. The points A, B, C and D are clearly shown in Figure 7(a).

Copyright © 2007 John Wiley & Sons, Ltd.

DOI: 10.1002/cnm

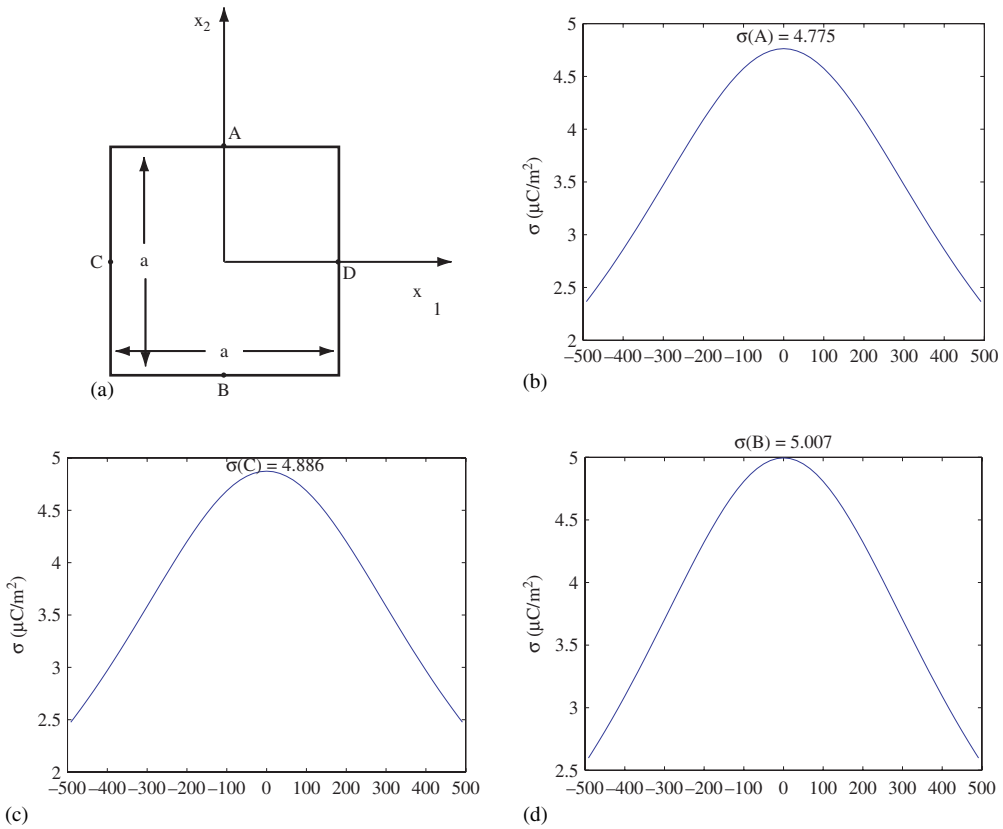


Figure 7. Charge density $\sigma$ per unit area around the central cross-section of the top beam. (a) Geometry and coordinate axes. (b)–(d) Charge density along top, left and bottom boundaries, respectively, of square cross-section of top beam. $\ell = 1000\,\mu$m, $g = 10\,\mu$m, $a = 1\,\mu$m. Two-beam model with $\phi_1 = 1$ V, $\tilde{\phi}_1 = -1$ V and $\varepsilon = 8.854 \times 10^{-12}$ F/m, and 401 quadratic elements along each beam.

Applying Equation (9), one gets:

$$\sigma(A) = \int_{s_1} \frac{\mathbf{r}(\mathbf{A},\mathbf{y}) \cdot \mathbf{n}(\mathbf{A}) q(\mathbf{y})}{4\pi r^3(A,\mathbf{y})}\, \mathrm{d}\ell(\mathbf{y}) - \int_{\tilde{s}_1} \frac{\mathbf{r}(\mathbf{A},\mathbf{y}) \cdot \mathbf{n}(\mathbf{A}) q(\mathbf{y})}{4\pi r^3(A,\mathbf{y})}\, \mathrm{d}\ell(\mathbf{y}) \tag{16}$$

With $q$ constant on an infinite tube (its value is given by (15)), using Figure 6, one has:

$$\begin{aligned}\sigma(A) &= \frac{q}{8\pi} \int_{-\infty}^{\infty} \frac{a\,\mathrm{d}z}{(z^2 + (a/2)^2)^{3/2}} - \frac{q}{4\pi} \int_{-\infty}^{\infty} \frac{(2g + 3(a/2))\,\mathrm{d}z}{[z^2 + (2g + 3(a/2))^2]^{3/2}} \\ &= \frac{q}{\pi a} - \frac{q}{2\pi}\left[\frac{1}{2g + 3(a/2)}\right] = \frac{q}{\pi a}\left[\frac{2g + a}{2g + 3(a/2)}\right]\end{aligned} \tag{17}$$

Copyright © 2007 John Wiley & Sons, Ltd.

DOI: 10.1002/cnm

Using a similar procedure, and noting that $\mathbf{r}(\mathbf{B}, \tilde{\mathbf{y}}) \cdot \mathbf{n}(\mathbf{B}) = -(2g + a/2)$ for $\tilde{\mathbf{y}} \in \tilde{s}_1$, one obtains

$$\sigma(B) = \frac{2q}{\pi a}\left[\frac{2g + a}{4g + a}\right] \tag{18}$$

Also

$$\sigma(C) = \sigma(D) = \frac{q}{\pi a}\left[\frac{a^2 + 4(2g + a)^2 - 1}{a^2 + 4(2g + a)^2}\right] \tag{19}$$

### *3.2. Numerical results for q for two parallel beams in Figure 2*

Numerical results, for the charge density $q$ per unit length, are presented in this section for two parallel beams of finite length (i.e. a narrow beam with its image in order to model the ground plane.) *The physical problem has narrow beams of nearly square cross-section, but these are replaced, for the computations, by beams of equivalent circular cross-section with the radius $\rho$ of each beam obtained from* (4). Also, for these calculations, $g_c + \rho = g + a/2$. for square and $g_c + \rho = g + b/2$ for rectangular cross-section beams. These results are then compared with the analytical solutions for infinite tubes (15) and also with numerical results from a standard 2-D BEM with two *square or rectangular* cross-sections (see Figure 4).

*3.2.1. Material and geometrical parameters.* The fixed values of the geometrical parameters are $\ell = 1000\,\mu\text{m}$ and $b = 1\,\mu\text{m}$ (for rectangular cross-sections). Other parameters are allowed to vary. Also, $\varepsilon = 8.854 \times 10^{-12}\,\text{F/m}$ and $\phi_1 = 1\,\text{V}$ and $\tilde{\phi}_1 = -1\,\text{V}$, respectively.

*3.2.2. Numerical results for square cross-section beams.* One-dimensional quadratic boundary elements are used to discretize each beam. The first and last boundary elements on a beam are nonconforming ones (with $\eta_1 = -0.5, \eta_2 = 0, \eta_3 = 1.0$; and $\eta_1 = -1.0, \eta_2 = 0, \eta_3 = 0.5$, respectively), to allow for singularities in $q$ at the two ends of the beam. (Here, $\eta$, with $-1 \leqslant \eta \leqslant 1$, is the intrinsic coordinate on a quadratic boundary element and $\eta_k$, $k = 1, 2, 3$, are its nodal values.) The rest of the elements are the usual quadratic conforming ones. Numerical results for $q_0$ (at the centre of the top beam), for different values of $g$ and $a$, respectively, are shown in Tables I and II. It is seen that the 3-D line model numerical results agree very well with the analytical solution (15). This serves to verify the computer code. More importantly, results from the 3-D line model are seen to agree quite well with the 2-D BEM results for a cross-section model—thus providing credibility to the line model for square cross-section beams proposed in this paper.

*3.2.3. Numerical results for rectangular cross-section beams.* Similar results for beams of rectangular cross-section appear in Table III. This time, $b = 1\,\mu\text{m}$ and $a$ is varied (see Figure 3). The radius $\rho$ of an equivalent circular cross-section beam is calculated from (4). The 3-D results agree very well with the analytical solution (15). (These analytical results are not reported in Table III.) The 2-D and 3-D results are seen to agree quite well for nearly square cross-section beams, but begin to diverge as the quantity $|a/b - 1|$ increases. This is expected since an equivalent circle is not able to adequately model aspect ratios far from unity, but is needed for the simplified BIE (5) to apply.

Copyright © 2007 John Wiley & Sons, Ltd.

DOI: 10.1002/cnm

Table I. Charge density $q_0$ at the centre of the upper narrow beam as a function of $g$ with $\ell = 1000\,\mu\text{m}$ and $a = 1\,\mu\text{m}$ ($\rho = 0.555\,\mu\text{m}$).

| $g$ (μm) | $q_0$ (pC/m)—3-D code computed | $q_0$ (pC/m)—analytical solution for $\ell_N \to \infty$ | $q_0$ (pC/m)—2-D code computed | Difference between 2-D and 3-D codes (%) |
|---|---|---|---|---|
| 10 | 15.32 | 15.32 | 15.65 | 2.1 |
| 20 | 12.94 | 12.93 | 13.17 | 1.75 |
| 50 | 10.71 | 10.69 | 10.85 | 1.3 |
| 100 | 9.50 | 9.44 | 9.57 | 0.73 |

*Note*: Two-beam model with $\phi_1 = 1\,\text{V}$, $\tilde{\phi}_1 = -1\,\text{V}$ and $\varepsilon = 8.854 \times 10^{-12}\,\text{F/m}$. Note that for the 3-D calculations, $g_c + \rho = g + a/2$ (see Figure 4), and 201 quadratic elements are used along each beam.

Table II. Charge density $q_0$ at the centre of the upper narrow beam as a function of $a$ with $\ell = 1000\,\mu\text{m}$ and $g = 100\,\mu\text{m}$.

| $a$ (μm) | $q_0$ (pC/m)—3-D code computed | $q_0$ (pC/m)—analytical solution for $\ell_N \to \infty$ | $q_0$ (pC/m)—2-D code computed | Difference between 2-D and 3-D codes (%) |
|---|---|---|---|---|
| 1 | 9.5 | 9.44 | 9.57 | 0.73 |
| 5 | 13.03 | 12.93 | 12.97 | 0.46 |
| 10 | 15.46 | 15.32 | 15.20 | 1.71 |
| 20 | 18.85 | 18.65 | 18.16 | 3.8 |

*Note*: Two-beam model with $\phi_1 = 1\,\text{V}$, $\tilde{\phi}_1 = -1\,\text{V}$ and $\varepsilon = 8.854 \times 10^{-12}\,\text{F/m}$. Note that for the 3-D calculations, $g_c + \rho = g + a/2$ (see Figure 4), and 201 quadratic elements are used along each beam.

Table III. Charge density $q_0$ at the centre of the upper narrow beam of rectangular cross-section, as a function of $a$ with $b = 1\,\mu\text{m}$, $\ell = 1000\,\mu\text{m}$ and $g = 10\,\mu\text{m}$.

| $a$ (μm) | $\rho$ (μm) | $q_0$ (pC/m)—3-D code computed | $q_0$ (pC/m)—2-D code computed | Difference between 2-D and 3-D codes (%) |
|---|---|---|---|---|
| 0.8 | 0.49 | 14.81 | 14.50 | 2.14 |
| 0.9 | 0.525 | 15.09 | 15.09 | 0 |
| 1.0 | 0.56 | 15.32 | 15.65 | 2.11 |
| 1.1 | 0.58 | 15.51 | 16.19 | 4.20 |
| 1.2 | 0.60 | 15.67 | 16.71 | 6.22 |

*Note*: Two-beam model with $\phi_1 = 1\,\text{V}$, $\tilde{\phi}_1 = -1\,\text{V}$ and $\varepsilon = 8.854 \times 10^{-12}\,\text{F/m}$. Note that for the 3-D calculations, $g_c + \rho = g + b/2$ (see Figure 4), and 201 quadratic elements are used along each beam.

### *3.3. Calculation of charge density σ on the surface of a narrow beam of square cross-section*

Two narrow beams with square cross-sections (Figure 4) are considered in this section. Again, the reader is reminded that square cross-section beams are considered here for illustrative purposes only. Analysis of rectangular cross-section beams requires only a simple extension of the ideas presented in this paper.

Copyright © 2007 John Wiley & Sons, Ltd.

DOI: 10.1002/cnm

Table IV. Charge density $\sigma$ at various points on the cross-section of the upper beam (see Figures 4 and 7).

| Point | $\sigma$ ($\mu$C/m$^2$) computed | $\sigma$ ($\mu$C/m$^2$) analytical | Difference (%) |
|---|---|---|---|
| A | 4.775 | 4.763 | 0.252 |
| B | 5.007 | 4.995 | 0.240 |
| C, D | 4.886 | 4.874 | 0.246 |

*Note*: $\ell = 1000\,\mu$m, $g = 10\,\mu$m, $a = 1\,\mu$m. Two-beam model with $\phi_1 = 1$ V, $\tilde{\phi}_1 = -1$ V and $\varepsilon = 8.854 \times 10^{-12}$ F/m, and 401 quadratic elements are used along each beam.

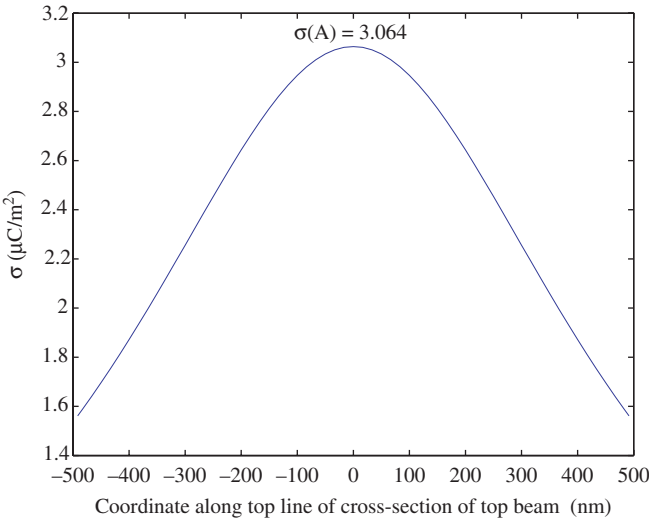


Figure 8. Charge density $\sigma$ per unit area along the top line of the central cross-section of top beam. $\ell = 1000\,\mu$m, $g = 100\,\mu$m, $a = 1\,\mu$m. Two-beam model with $\phi_1 = 1$ V, $\tilde{\phi}_1 = -1$ V and $\varepsilon = 8.854 \times 10^{-12}$ F/m, and 401 quadratic elements along each beam.

Figure 7 shows plots for $\sigma$ on various segments of the boundary of the central cross-section of the upper beam. These numerical results are obtained from the gradient BIE (9) (see also (14)).

Comparisons of numerical solutions for $\sigma$ at the points A, B, C and D, with analytical results from (17) to (19), appear in Table IV. The numerical results are seen to be very accurate.

Finally, similar results for a gap $g = 100\,\mu$m are shown in Figure 8. This time, the analytical solution from (17) is 2.997 $\mu$C/m$^2$.

## 4. A CONCLUDING REMARK

A line model for a nanotube of circular cross-section [25] is extended in this paper to narrow MEMS beams of rectangular (nearly square) cross-section. This proposed model is very much simpler

Copyright © 2007 John Wiley & Sons, Ltd.

DOI: 10.1002/cnm

than a full BIE model (see, e.g. [24]). Numerical results presented in this paper are encouraging for beams with rectangular cross-sections whose aspect ratios are not far from unity. Based on the results presented in this paper, it is suggested that this approach is useful for rectangular beams with aspect ratios $0.8 \leqslant a/b \leqslant 1.2$.

This paper complements earlier work on thin plates [19, 22] and beams [20]. The 2-D model in [20] is valid for beams of rectangular cross-section with large aspect ratios, while the present work applies to narrow beams of nearly square cross-section.

## ACKNOWLEDGEMENT

This research has been supported by Grant # CMS-0508466 of the National Science Foundation to Cornell University.

## REFERENCES

1. Mukherjee S. *Boundary Element Methods in Creep and Fracture*. Applied Science Publishers: London, 1982.
2. Banerjee PK. *The Boundary Element Methods in Engineering*. McGraw-Hill Europe: Maidenhead, Berkshire, England, 1994.
3. Chandra A, Mukherjee S. *Boundary Element Methods in Manufacturing*. Oxford University Press: New York, 1997.
4. Bonnet M. *Boundary Integral Equation Methods for Solids and Fluids*. Wiley: Chichester, U.K., 1999.
5. Mukherjee S, Mukherjee YX. *Boundary Methods*: *Elements Contours and Nodes*. Taylor & Francis, CRC Press: London, Boca Raton, FL, 2005.
6. Yang TY. *Finite Element Structural Analysis*. Prentice-Hall: Englewood Cliffs, NJ, 1986.
7. Zienkiewicz OC, Taylor RL. *The Finite Element Method*, vols. 1 and 2 (4th edn). McGraw-Hill: Maidenhead, Berkshire, U.K., 1994.
8. Hughes TJR. *The Finite Element Method*: *Linear Static and Dynamic Finite Element Analysis*. Dover: Mineola, NY, 2000.
9. Senturia SD, Harris RM, Johnson BP, Kim S, Nabors K, Shulman MA, White JK. A computer-aided design system for microelectromechanical systems (MEMCAD). *Journal of Microelectromechanical Systems* 1992; **1**:3–13.
10. Nabors K, White J. FastCap: a multi-pole accelerated 3-D capacitance extraction program. *IEEE Transactions on Computer Aided Design and Integrated Circuits and Systems* 1991; **10**:1447–1459.
11. Gilbert JR, Legtenberg R, Senturia SD. 3D coupled electromechanics for MEMS: applications of CoSolve-EM. *Proceedings of the IEEE MEMS*, Amsterdam, The Netherlands, 1995; 122–127.
12. Shi F, Ramesh P, Mukherjee S. Simulation methods for micro-electro-mechanical structures (MEMS) with application to a microtweezer. *Computers and Structures* 1995; **56**:769–783.
13. Aluru NR, White J. An efficient numerical technique for electromechanical simulation of complicated microelectromechanical structures. *Sensors and Actuators A* 1997; **58**:1–11.
14. Mukherjee S, Bao Z, Roman M, Aubry N. Nonlinear mechanics of MEMS plates with a total Lagrangian approach. *Computers and Structures* 2005; **83**:758–768.
15. Shi F, Ramesh P, Mukherjee S. Dynamic analysis of micro-electro-mechanical systems. *International Journal for Numerical Methods in Engineering* 1996; **39**:4119–4139.
16. De SK, Aluru NR. Full-Lagrangian schemes for dynamic analysis of electrostatic MEMS. *Journal of Microelectromechanical Systems* 2004; **13**:737–758.
17. Frangi A, di Gioia A. Multipole BEM for the evaluation of damping forces on MEMS. *Computational Mechanics* 2005; **37**:24–31.
18. Harrington RF. *Field Computation by Moment Methods*. IEEE Press: Piscataway, NJ, 1993.
19. Bao Z, Mukherjee S. Electrostatic BEM for MEMS with thin conducting plates and shells. *Engineering Analysis with Boundary Elements* 2004; **28**:1427–1435.
20. Bao Z, Mukherjee S. Electrostatic BEM for MEMS with thin beams. *Communications in Numerical Methods in Engineering* 2005; **21**:297–312.
21. Chuyan SW, Liao YS, Chen JT. Computational study of the effect of finger width and aspect ratios for the electrostatic levitating force of MEMS combdrive. *Journal of Microelectromechanical Systems* 2005; **14**:305–312.

Copyright © 2007 John Wiley & Sons, Ltd.

DOI: 10.1002/cnm

22. Telukunta S, Mukherjee S. Fully Lagrangian modeling of MEMS with thin plates. *Journal of Microelectromechanical Systems* 2006; **15**:795–810.
23. Mukherjee S, Telukunta S, Mukherjee YX. BEM modeling of damping forces on MEMS with thin plates. *Engineering Analysis with Boundary Elements* 2005; **29**:1000–1007.
24. Ke C, Espinosa HD. Numerical analysis of nanotube-based NEMS devices—Part I: Electrostatic charge distribution on multiwalled nanotubes. *Journal of Applied Mechanics* (ASME) 2005; **72**:721–725.
25. Chen H, Mukherjee S. Charge distribution on thin conducting nanotubes—reduced 3-D model. *International Journal for Numerical Methods in Engineering* 2006; **68**:503–524.
26. Batra RC, Porfiri M, Spinello D. Electromechanical model of electrically actuated narrow microbeams. *Journal of Microelectromechanical Systems* 2006; **15**:1175–1189.
27. Chen H, Mukherjee S. Modeling of the ground plane in electrostatic BEM analysis of MEMS and NEMS. *Engineering Analysis with Boundary Elements* 2006; **30**:910–924.
28. Hayt W, Buck J. *Engineering Electromagnetics* (6th edn). McGraw-Hill: New York, 2001.

Copyright © 2007 John Wiley & Sons, Ltd.

DOI: 10.1002/cnm